Integrated optical cross strip polarizer concept

Manfred Lohmeyer, Remco Stoffer*

MESA+ Research Institute, University of Twente, Enschede, The Netherlands

Abstract: Passing across an abrupt junction from a thick vertically bimodal waveguide to a thinner single mode segment, guided light can undergo complete destructive interference, provided that the geometry and the phases of the modes in the initial segment are properly adjusted. We propose to employ this effect to realize a simple polarizer configuration, using a strip that is etched from a planar waveguide. A beam of light is made to pass the strip perpendicularly. The light enters from the single mode waveguide outside the strip into the strip segment, which is configured to support two modes. At the end of the strip, apart from reflections, the amount of power that is guided in the following lower segment depends on the local phases of the two modes. These phases are different for TE and TM light, hence we may expect a polarization dependent power transfer, resulting in polarizer performance for a properly selected geometry. The paper describes in detail the modeling of the device in terms of rigorous mode expansion. Design guidelines and tolerance requirements for geometric and material parameters are discussed. For typical Si_3N_4/SiO_2 materials, our calculations predict a peak performance of $34\,dB$ polarization discrimination and $0.3\,dB$ insertion loss for a device with a total length of about $12\,\mu$m that selects TE polarization at a wavelength of $1.3\,\mu$m.

1 Introduction

Planar or quasiplanar waveguides based on higher refractive index films between substrate and cover layers with lower refractive index form the basic element for most integrated optical circuits. Even if the involved materials are isotropic, guided fields of different polarizations propagate at different phase velocities; hence almost all devices relying on mode interference are sensitive to the light polarization. Where an optimization aiming at a polarization independent performance (e.g. by a compensation of polarization effects) or parallel light processing (by applying polarization splitters) is complicated, impossible, or unnecessary, the device is usually restricted to single polarization operation. This necessarily involves the inclusion of polarizers.

Most concepts for guided wave polarizers are based on trying to exclusively attenuate one of the basic TE or TM modes. Among the variety of proposals are overlays of strongly absorbing, metallic [1, 2] or amorphous [3, 4] materials, the inclusion of metallic thin films [5, 6, 7], or thin composite, highly dichromatic metallic layers [8, 9, 10], and highly refracting or birefringent transparent overlays [11, 12, 13]. Alternatively, the overlays can be substituted by parallel waveguide segments [14, 15]. A number of interferometric concepts for polarization splitters employ directional couplers [16, 17], Mach-Zehnder interferometers [18, 19], other multiwaveguide geometries [20, 21, 22], or recently a birefringent Y-junction [23]. Besides in terms of polarization discrimination and insertion loss, an integrated device must be rated with respect to its length. Since a polarizer is usually not meant as a device of its own, but as a component of a larger circuit, the design should be adaptable to a large variety of basic material systems, requiring no extra materials or complicated processing steps at best.

In this paper we address the task using a particularly simple kind of interferometer. Figure 1 sketches the geometry of the planar configuration and introduces the relevant dimensional and material parameters. Depending on the technological framework, the design should be an alternative to the formerly referenced concepts with respect to either of the above criteria, provided that only polarizer performance is desired.

Following the introduction of some notation and basic relations in Section 2, the analysis in Section 3 starts with a basic overlap model of the interferometer involving only forward traveling guided modes. In Section 4 we take a closer look at the two waveguide junctions by means of a rigorous approach that includes reflected

---

* Faculty of Mathematical Sciences, University of Twente   *P.O. Box 217, 7500 AE Enschede, The Netherlands*
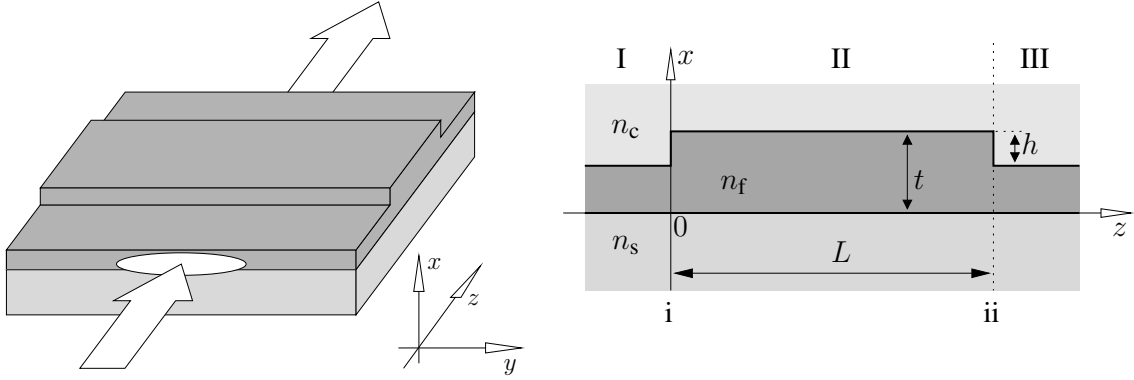*Phone: +31/53/489-3448*   *Fax: +31/53/489-4888*   *E-mail: m.lohmeyer@math.utwente.nl*

Figure 1: The planar waveguide configuration. x and y denote the cross section coordinate axes, with the x-direction normal to the film plane. Light propagates along the z-direction, perpendicularly to a wide strip that has been etched into the guiding film. n_s, n_f, and n_c are the refractive indices of the substrate, the film, and the cover; the geometry is fixed in terms of the total film thickness t, the etching depth h, and the length L of the thick segment. Roman numbers I, II, III, and i, ii identify the three longitudinally homogeneous waveguide sections and the two junctions at $z = 0$ and $z = L$, respectively.

and radiated parts of the field on a computational window of suitable extension. Additionally, the results are verified by a comparison with time domain beam propagation simulations that are completely independent from the former modeling.

Subsequently, Section 5 considers the entire structure again. The mode expansion on a finite window can still be formulated quite rigorously, if one assumes that only guided modes are responsible for the forward and backward power transfer between the junctions. Finally, Section 6 sketches the optimization procedure for the polarizer and shows a simulation of the resulting device.

2 Mode expansion

The structure under investigation consists of three longitudinally homogeneous waveguide sections. Hence the local electromagnetic field is assumed to be a superposition of modes, i.e. electric $\mathcal{E}$ and magnetic fields $\mathcal{H}$ of the form (in common complex notation)

$$\mathcal{E}(x, z, t) = \boldsymbol{E}(x)\, \mathrm{e}^{\mathrm{i}\omega t - \mathrm{i}\beta z}, \quad \mathcal{H}(x, z, t) = \boldsymbol{H}(x)\, \mathrm{e}^{\mathrm{i}\omega t - \mathrm{i}\beta z}. \tag{1}$$

$\boldsymbol{E}$ and $\boldsymbol{H}$ are the complex electric and magnetic parts of the mode profile, β denotes the corresponding propagation constant. The frequency ω is usually given in terms of the vacuum wavelength $\lambda = 2\pi \mathrm{c}/\omega$, where c is the speed of light in vacuum. The modeling shall be restricted to two spatial coordinates, with the permittivity and the fields assumed to be constant in the y-direction. A solution of the Maxwell equations in the form (1) is called a forward traveling propagating mode, if $\beta > 0$. A backward traveling propagating mode satisfies $\beta < 0$. The corresponding mode profiles can be chosen such that the transverse components E_x, E_y, H_x, and H_y are real, while E_z and H_z are imaginary. Evanescent modes have imaginary propagation constants $\beta = -\mathrm{i}\alpha$, with real α. Those with $\alpha > 0$, i.e. in positive z-direction exponentially decreasing fields, shall be called forward traveling, others with $\alpha < 0$ are called backward traveling. Here all electric components of the mode profile may be real, while the magnetic components are purely imaginary.

For convenience we collect the in general six components of a mode profile into a single quantity $\boldsymbol{\psi}_m^s$. If applicable, it is decorated with a superscript $s \in \{\mathrm{I}, \mathrm{II}, \mathrm{III}\}$ that identifies the waveguide segment to which the mode belongs, and by a subscript m that specifies the mode index. This notation transfers to the propagation constant β_m^s and to the parts of the mode profile. For this paper, only configurations with numerable sets $\{\boldsymbol{\psi}_l^{\mathrm{I}}\}$, $\{\boldsymbol{\psi}_m^{\mathrm{II}}\}$, $\{\boldsymbol{\psi}_n^{\mathrm{III}}\}$, are of interest, either because the discussion is restricted to guided fields, or because the mode spectrum is discretized by using a finite transverse computational window.

For each mode with profile $\boldsymbol{\psi}$ and propagation constant β a mode can be constructed, which travels in the opposite direction. The profile $\boldsymbol{\psi}^{\mathrm{r}}$ has the E_z, H_x, and H_y components multiplied by -1, the propagation

constant is $\beta^{\text{r}} = -\beta$. If relevant, forward and backward traveling modes will be given upper indices f and b, respectively. In that case, the numbering shall be applied separately to forward and backward propagating modes, such that $\boldsymbol{\psi}_m^{s,\text{b}} = (\boldsymbol{\psi}_m^{s,\text{f}})^{\text{r}}$.

Since this deals with planar structures, the mode spectrum splits into a TE part, where only the E_y, H_x, and H_z components are present in the mode profiles, and into a second TM part, where these components of the mode profiles vanish. Occasionally, an additional index TE or TM indicates the polarization.

For purposes of field decomposition and power summation, we employ the following product of two general electromagnetic fields $\boldsymbol{\psi} = (\boldsymbol{E}_1, \boldsymbol{H}_1)$ and $\boldsymbol{\phi} = (\boldsymbol{E}_2, \boldsymbol{H}_2)$:

$$(\boldsymbol{\psi}; \boldsymbol{\phi}) = (\boldsymbol{E}_1, \boldsymbol{H}_1; \boldsymbol{E}_2, \boldsymbol{H}_2) = \frac{1}{4} \int \left(E_{1x}^* H_{2y} - E_{1y}^* H_{2x} + E_{2x} H_{1y}^* - E_{2y} H_{1x}^* \right) \mathrm{d}x \,. \tag{2}$$

Here the asterisk denotes complex conjugation. Note that (2) combines only the transverse electric and magnetic components.

Defining the mode powers

$$P_m^s = \begin{cases} \left| (\boldsymbol{\psi}_m^s; \boldsymbol{\psi}_m^s) \right|, & \text{if mode } m \text{ is propagating,} \\ \left| (\boldsymbol{\psi}_m^s; (\boldsymbol{\psi}_m^s)^{\text{r}}) \right|, & \text{if mode } m \text{ is evanescent,} \end{cases} \tag{3}$$

the following orthogonality relations hold for uniformly polarized modes belonging to the same segment s:

$$\left.\begin{aligned} (\boldsymbol{\psi}_l^{s,\text{f}}; \boldsymbol{\psi}_m^{s,\text{f}}) &= \delta_{lm} P_m^s \,, \\ (\boldsymbol{\psi}_l^{s,\text{b}}; \boldsymbol{\psi}_m^{s,\text{b}}) &= -\delta_{lm} P_m^s \,, \\ (\boldsymbol{\psi}_l^{s,\text{f}}; \boldsymbol{\psi}_m^{s,\text{b}}) &= (\boldsymbol{\psi}_l^{s,\text{b}}; \boldsymbol{\psi}_m^{s,\text{f}}) = 0 \,, \end{aligned}\right\} \text{if mode } m \text{ is propagating,}$$

$$\left.\begin{aligned} (\boldsymbol{\psi}_l^{s,\text{f}}; \boldsymbol{\psi}_m^{s,\text{b}}) &= \pm\mathrm{i}\,\delta_{lm} P_m^s \,, \\ (\boldsymbol{\psi}_l^{s,\text{b}}; \boldsymbol{\psi}_m^{s,\text{f}}) &= \mp\mathrm{i}\,\delta_{lm} P_m^s \,, \\ (\boldsymbol{\psi}_l^{s,\text{f}}; \boldsymbol{\psi}_m^{s,\text{f}}) &= (\boldsymbol{\psi}_l^{s,\text{b}}; \boldsymbol{\psi}_m^{s,\text{b}}) = 0 \,, \end{aligned}\right\} \text{if mode } m \text{ is evanescent.} \tag{4}$$

$\delta_{lm} = 1$, if $l = m$, otherwise $\delta_{lm} = 0$. The statements imply that products between a propagating and an evanescent mode vanish. The upper signs in the fourth and fifth line of Eq. (4) apply to TE polarized fields, the lower to the TM case.

As a consequence, the total power $\mathcal{P}^s = \operatorname{Re} \int (\boldsymbol{\mathcal{E}}^s \times (\boldsymbol{\mathcal{H}}^s)^*)_z \, \mathrm{d}x/2$ (the integrated longitudinal component of the Poynting-vector) attributed to the mode superposition

$$\begin{pmatrix} \boldsymbol{\mathcal{E}} \\ \boldsymbol{\mathcal{H}} \end{pmatrix}^s (x, z, t) = \sum_m F_m^s \frac{1}{\sqrt{P_m^s}} \boldsymbol{\psi}_m^{s,\text{f}}(x) \, \mathrm{e}^{\mathrm{i}\omega t - \mathrm{i}\beta_m^s z} \; + \; \sum_m B_m^s \frac{1}{\sqrt{P_m^s}} \boldsymbol{\psi}_m^{s,\text{b}}(x) \, \mathrm{e}^{\mathrm{i}\omega t + \mathrm{i}\beta_m^s z} \tag{5}$$

in waveguide segment s is

$$\mathcal{P}^s = \sum_{m,\text{propag.}} \left(|F_m^s|^2 - |B_m^s|^2 \right) \; \pm \; \mathrm{i} \sum_{m,\text{evanesc.}} \left((F_m^s)^* B_m^s - F_m^s (B_m^s)^* \right) \,. \tag{6}$$

This clarifies at least the naming 'forward' and 'backward' for the propagating modes, which are included in the first summation. Forward / backward traveling evanescent modes are in the positive z-direction exponentially decreasing or increasing fields, respectively. A — longitudinally constant — contribution to the total power does only arise, if both types are present simultaneously.

In the derivation of Eq. (6), one rewrites $\mathcal{P}^s$ as $\mathcal{P}^s = (\boldsymbol{\mathcal{E}}, \boldsymbol{\mathcal{H}}; \boldsymbol{\mathcal{E}}, \boldsymbol{\mathcal{H}})$. Observing that expression (2) vanishes $(\boldsymbol{\psi}^{\text{TE}}; \boldsymbol{\psi}^{\text{TM}}) = 0$ with a TE field $\boldsymbol{\psi}^{\text{TE}}$ and a TM field $\boldsymbol{\psi}^{\text{TM}}$ inserted (even if the modes do *not* belong to the same waveguide), this justifies completely separated simulations for TE and TM polarization: TE and TM modes do not interfere, the powers related to both polarizations may be computed separately, and added afterwards. While this applies only to homogeneous segments, e.g. by reading through the following paragraphs one can

quickly check that transisitions between adjacent waveguide sections can be (rigorously) expressed in terms of products (2) between the local modes on both sides. Hence there is no interaction between the polarizations at the junctions likewise.

Naturally, the mode expansion technique initiated in this section resembles the formulations given e.g. in Refs. [24, 25, 26]. However, for a polarizer design we necessarily have to consider both polarizations. The present formalism applies to the TE and TM cases, which are dealt with separately in the two latter references. The more abstract approach in terms of general modes and products of modes, rather than handling the scalar basic components of TE and TM fields, has turned out to be very convenient for the numerical implementation. In particular, it enables a compact formulation of the propagating mode analysis for the long cross strip segment.

3 Cross strip interferometer: Overlap model

Assuming that only the forward traveling guided modes are present, the total fields in the three waveguide segments are given by expression (5), restricted to the single input and output terms ψ_0^{I}, ψ_0^{III} in sections I, III, and to the two guided modes ψ_0^{II}, ψ_1^{II} of the strip segment (the superscript f will be suppressed here). Given the input mode amplitude F_0^{I} in terms of the input power $\mathcal{P}^{\mathrm{I}} = |F_0^{\mathrm{I}}|^2$, we are interested in the intermediate amplitudes F_0^{II}, F_1^{II}, and in the output power $\mathcal{P}^{\mathrm{III}} = |F_0^{\mathrm{III}}|^2$.

Since the transverse electric and magnetic fields are required to be continuous on the planes of the junctions, putting the local expressions for the adjacent fields equal allows to extract the outgoing mode amplitudes by projecting on the incoming fields. Note that only the x- and y-components which are tangential to the z-discontinuity may be set equal. But only these are required to evaluate (2). Provided that the fields on both sides satisfy the Maxwell equations, the curl relations imply the continuity of the z-components of the magnetic field and of the dielectric displacement.

For junction i, the projection yields

$$F_m^{\mathrm{II}} = F_0^{\mathrm{I}} \frac{(\psi_m^{\mathrm{II}}; \psi_0^{\mathrm{I}})}{\sqrt{P_m^{\mathrm{II}} P_0^{\mathrm{I}}}}\,, \quad m = 0, 1\,. \tag{7}$$

Using identical modes $\psi_0^{\mathrm{III}} = \psi_0^{\mathrm{I}}$ for the input and output segments, the output power evaluates to

$$\mathcal{P} = \mathcal{P}^{\mathrm{III}} = \mathcal{P}^{\mathrm{I}} \left(w_0^2 + w_1^2 + 2 w_0 w_1 \cos(\beta_0^{\mathrm{II}} - \beta_1^{\mathrm{II}}) L \right) \quad \text{with} \quad w_m = \frac{\left| (\psi_m^{\mathrm{II}}; \psi_0^{\mathrm{I}}) \right|^2}{P_m^{\mathrm{II}} P_0^{\mathrm{I}}}\,. \tag{8}$$

$\mathcal{P}$ varies harmonically[†] with the strip length L, oscillating between the maximum value $\mathcal{P}^{\mathrm{I}}(w_0 + w_1)^2$ and the minimum $\mathcal{P}^{\mathrm{I}}(w_0 - w_1)^2$ with the half-beat length or coupling length $L_{\mathrm{c}} = \pi/(\beta_0^{\mathrm{II}} - \beta_1^{\mathrm{II}})$. The maximum (minimum) power is transfered if L matches an even (odd) multiple of L_{c}.

Consequently, the model predicts a vanishing throughput, if one can dimension the waveguides such that $w_0 = w_1$, which must be considered a major requirement for the interferometer. According to Eq. (7), the incoming power is then equally distributed between ψ_0^{II} and ψ_1^{II} at junction i. In the cases of extremal power transfer, these modes excite junction ii with equal absolute amplitudes, but with zero relative phase difference, or with a difference of π, respectively.

For a certain range of thicknesses t we have found that a dimensioning aiming at $w_0 = w_1$ is indeed possible by choosing a proper etching depth h. The freedom in the strip thickness t can be exploited to optimize $w_0 + w_1$, i.e. the maximum power throughput. Figure 2 shows examples for the resulting mode profiles and the relevant superpositions. Note that in general the thickness tuning is not possible simultaneously for TE and TM polarized light.

[†]Precisely this variation has been observed in Ref. [2] in the framework of an investigation concerning metal clad waveguide polarizers. But, regarded as an undesired feature, the effect was not further exploited.
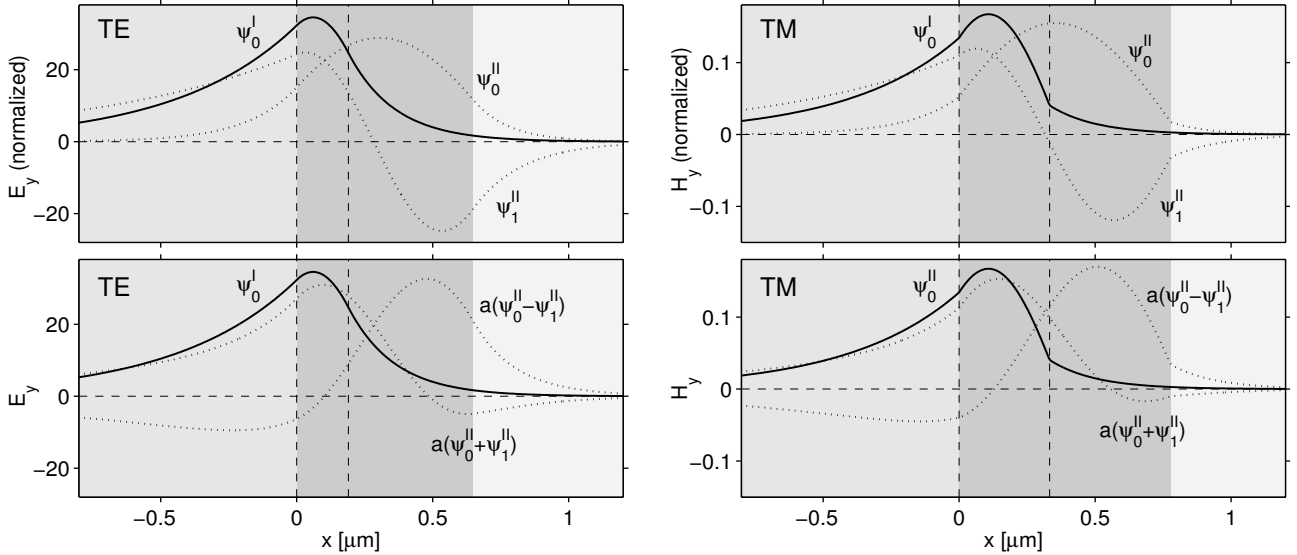
Figure 2: *For structures defined by the material parameters and wavelength of Table 2 with thicknesses and etching depths $t = 0.6499\,\mu m$, $h = 0.4598\,\mu m$ (TE, left column) and $t = 0.7778\,\mu m$, $h = 0.4449\,\mu m$ (TM, right column):*
Top: Basic field components E_y (TE) and H_y (TM) of the modes ψ_0^I of the input/output waveguide, and the profiles coresponding to ψ_0^{II}, ψ_1^{II} in the coupling segment. Bottom: With suitable amplitudes $a = F_m^{II} = \sqrt{w_m} = 0.689$ (TE) and 0.694 (TM), for unit input power, the modes of the thicker waveguide form fields $a(\psi_0^{II} - \psi_1^{II})$ that are orthogonal to the output profile, or fields $a(\psi_0^{II} + \psi_1^{II})$ that are reasonably close to the output modes. The shading indicates the permittivity of the coupling segment, while the vertical lines mark the boundaries of the input/output core.

While optimized for a vanishing minimum power transfer, the parameters given for Figure 2 yield a maximum relative throughput $(w_0 + w_1)^2 = (2a^2)^2$ of 90% (TE) and 93% (TM). One can observe, that these losses are much lower for other material parameters or basic geometries, e.g. if one forms the cross strip in a two layered guiding film with a slightly increased refractive index of the top layer[‡]. However, since the polarizer design should be as simple as possible and adaptable to the underlying circuit, where the additional layer won't fit, for this paper we stick to the single layer configuration.

4 Waveguide junction: Mode expansion

Since totally neglecting the influence of radiation and reflection at the abrupt waveguide junctions may be expected to be insufficient, we consider the junctions a second time, now including these effects by expanding into a larger mode set. For this purpose, the interesting region on the x-axis is enclosed by a computational window. The mode spectrum becomes discrete, if the basic mode components (E_y for TE, H_y for TM polarization) are set to zero on the window boundaries. If these are sufficiently far apart, such that the guided exciting and outgoing fields can well be neglected beyond the boundaries, in the plane of the junction the total electromagnetic field will be localized around the waveguide, with radiated fields approaching the boundaries only at some distance from the junction. By virtue of the orthogonality relations (4), one may expect correct results for the reflection and transmission coefficients of the guided modes in the limit of many terms in the mode decomposition, even with a finite window. Close to the junction, where reflections from the window boundaries are not relevant, the field computed in this way should be a good approximation to the field in the open structure.

Again the electromagnetic field on both sides of junction i is searched in the form (5), now with forward and backward, propagating and evanescent terms present. Using (2) on the equated transverse components, projection onto either segment I or segment II allows one to extract the mode amplitudes. The mode overlaps

---

[‡]A two layered structure made of garnet materials (bottom layer: refractive index 2.157, thickness $0.656\,\mu m$, top layer: refractive index 2.275, thickness $0.559\,\mu m$, substrate: refractive index 1.95, cover: air, etching depth $0.405\,\mu m$) allows for vanishing minimum power transfer with a maximum throughput of 98%, for TM polarized light at a wavelength of $1.3\,\mu m$.

are stored in the matrices

$$(\mathsf{D}^s_{\mu\nu})_{lm} = (\boldsymbol{\psi}^{s,\mu}_l; \boldsymbol{\psi}^{s,\nu}_m) \quad \text{and} \quad (\mathsf{O}_{\mu\nu})_{lm} = (\boldsymbol{\psi}^{\mathrm{II},\mu}_l; \boldsymbol{\psi}^{\mathrm{I},\nu}_m), \tag{9}$$

where indices $s = \mathrm{I}, \mathrm{II}$ specify the segment, $\mu, \nu = \mathrm{f}, \mathrm{b}$ identify a propagation direction, and l, m extend over the range of the terms in the mode expansions. Putting additionally the mode normalizations into the amplitudes $f^s_m = F^s_m / \sqrt{P^s_m}$, $b^s_m = B^s_m / \sqrt{P^s_m}$ and combining these to amplitude vectors $\boldsymbol{f}^s$, $\boldsymbol{b}^s$, one finds the latter related as

$$\begin{pmatrix} \boldsymbol{f}^{\mathrm{I}} \\ \boldsymbol{b}^{\mathrm{I}} \end{pmatrix} = \mathsf{M}^{\mathrm{I}} \begin{pmatrix} \boldsymbol{f}^{\mathrm{II}} \\ \boldsymbol{b}^{\mathrm{II}} \end{pmatrix}, \quad \begin{pmatrix} \boldsymbol{f}^{\mathrm{II}} \\ \boldsymbol{b}^{\mathrm{II}} \end{pmatrix} = \mathsf{M}^{\mathrm{II}} \begin{pmatrix} \boldsymbol{f}^{\mathrm{I}} \\ \boldsymbol{b}^{\mathrm{I}} \end{pmatrix}, \tag{10}$$

with transfer matrices M^s given by

$$\mathsf{M}^{\mathrm{I}} = (\mathsf{D}^{\mathrm{I}})^{-1}\mathsf{O}^*, \quad \mathsf{M}^{\mathrm{II}} = (\mathsf{D}^{\mathrm{II}})^{-1}\mathsf{O}, \quad \text{for} \quad \mathsf{D}^s = \begin{pmatrix} \mathsf{D}^s_{\mathrm{ff}} & \mathsf{D}^s_{\mathrm{fb}} \\ \mathsf{D}^s_{\mathrm{bf}} & \mathsf{D}^s_{\mathrm{bb}} \end{pmatrix}, \quad \mathsf{O} = \begin{pmatrix} \mathsf{O}_{\mathrm{ff}} & \mathsf{O}_{\mathrm{fb}} \\ \mathsf{O}_{\mathrm{bf}} & \mathsf{O}_{\mathrm{bb}} \end{pmatrix}. \tag{11}$$

Here the asterisk denotes the adjoint matrix.

If one considers the single junction i excited by the forward traveling modes on left segment, then $\boldsymbol{f}^{\mathrm{I}}$ (the input amplitudes) is prescribed, $\boldsymbol{b}^{\mathrm{I}}$ (the reflection coefficients) and $\boldsymbol{f}^{\mathrm{II}}$ (the transmission coefficients) are unknowns, and $\boldsymbol{b}^{\mathrm{II}}$ is zero (there is no light coming in from the right). Splitting now M^s as

$$\mathsf{M}^s = \begin{pmatrix} \mathsf{M}^s_{\mathrm{ff}} & \mathsf{M}^s_{\mathrm{fb}} \\ \mathsf{M}^s_{\mathrm{bf}} & \mathsf{M}^s_{\mathrm{bb}} \end{pmatrix}, \tag{12}$$

the unknown mode transmissions and reflections can be computed:

$$\boldsymbol{f}^{\mathrm{II}} = \left(1 - \mathsf{M}^{\mathrm{II}}_{\mathrm{fb}}\mathsf{M}^{\mathrm{I}}_{\mathrm{bf}}\right)^{-1} \mathsf{M}^{\mathrm{II}}_{\mathrm{ff}}\boldsymbol{f}^{\mathrm{I}}, \quad \boldsymbol{b}^{\mathrm{I}} = \mathsf{M}^{\mathrm{I}}_{\mathrm{bf}}\boldsymbol{f}^{\mathrm{II}}, \quad F^s_m = \sqrt{P^s_m}\, f^s_m, \quad B^s_m = \sqrt{P^s_m}\, b^s_m. \tag{13}$$

Note that this formalism does not require the number of expansion terms in segments I and II to be equal [24], in contrast to the formulations in Refs. [25, 26].

Figure 3 illustrates the results for the parameters found to be interesting in the last section (the data of Figure 2). The plane of junction ii has been shifted to the origin, where we have to stretch the notation somewhat with respect to the numbering of the segments. Only the forward traveling guided fields on the left of the junctions are incident: $F^{\mathrm{I}}_0 = 1$ in (a), $F^{\mathrm{II}}_0 = \pm F^{\mathrm{II}}_1 = 1/\sqrt{2}$ in (b) and (c), respectively; the remaining entries in $\boldsymbol{f}^{\mathrm{I}}$ or $\boldsymbol{f}^{\mathrm{II}}$ were set to zero. For a more quantitative assessment, Table 1 summarizes the relative mode powers of the reflected and transmitted guided fields. The mode expansion simulations use 400 terms on each side of the junctions, on a computational window extending from $x = -15\,\mu\mathrm{m}$ to $x = 10\,\mu\mathrm{m}$. The given values are found to be converged with respect to enlarging the window and to increasing the number of expansion terms.

Despite its simplicity, the predictions of the overlap model of Section 3 turn out to be surprisingly good: At junction i (a), the modes $\boldsymbol{\psi}^{\mathrm{II}}_0$ and $\boldsymbol{\psi}^{\mathrm{II}}_1$ receive almost half of the incoming power each. If the symmetric superposition of these modes arrives at junction ii (b), this leads to constructive interference with most of the power remaining guided in segment III. In both cases (a) and (b) only very small amounts of power are reflected into the guided fields. The antisymmetric superposition causes destructive interference (c). Here the largest part of the power is radiated away from the core in segment III, dominantly into the substrate region. Another part radiates backwards into segment II. And a certain amount is reflected into the backward traveling guided modes, which will have to play a role in the following section.

The number of 400 expansion terms, chosen to generate sound reference values, may seem to be unnecessarily large. If interest is in the reflection and transmission coefficients of the guided modes only, then indeed digits like those given in Table 1(c),TM can be produced with a much smaller computational window of $-2.4\,\mu\mathrm{m} \leq x \leq 2.2\,\mu\mathrm{m}$ and only 20 terms in the mode expansions (which includes already 11 (10) evanescent modes for the thin (thick) segment). On the other hand, plots like Figure 3(c) drawn from that computation appear
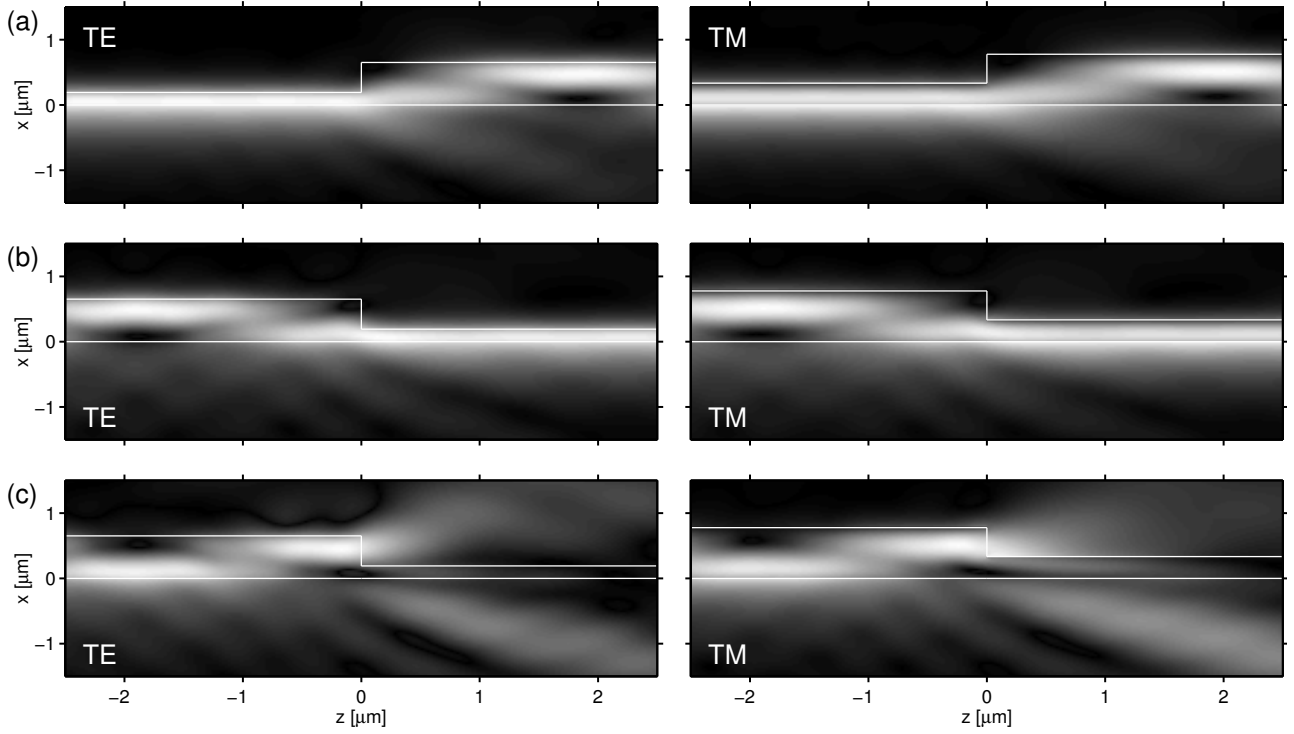
Figure 3: Simulations of the light propagation through the separated waveguide junctions i and ii, with parameters as given for Figure 2 and Table 1. The left and right comlumns display TE and TM polarized fields, where the gray scale levels correspond to the squareroot of the z-component of the local Poynting vector. (a): Transition $I \to II$; Input: the single mode of the thin segment. (b): Transition $II \to III$; Input: the positive superposition of the two modes of the thick segment (see Figure 2). (c): Transition $II \to III$; Input: the superposition with the negative sign. In case of two initially excited modes, the term 'input' means that the two modes are lauched to arrive at the junction with proper amplitudes and phases.

(a) Junction i, $F_0^I = 1$:

	TE, $\lvert B_0^I\rvert^2$	TE, $\lvert F_0^{II}\rvert^2$	TE, $\lvert F_1^{II}\rvert^2$	TM, $\lvert B_0^I\rvert^2$	TM, $\lvert F_0^{II}\rvert^2$	TM, $\lvert F_1^{II}\rvert^2$
ME	$5.2 \cdot 10^{-4}$	0.46	0.49	$1.3 \cdot 10^{-4}$	0.46	0.50
FDTD	$5.1 \cdot 10^{-4}$	0.47	0.48	$1.0 \cdot 10^{-4}$	0.45	0.52

(b) Junction ii, $F_0^{II} = 1/\sqrt{2}$, $F_1^{II} = 1/\sqrt{2}$:

	TE, $\lvert B_0^{II}\rvert^2$	TE, $\lvert B_1^{II}\rvert^2$	TE, $\lvert F_0^{III}\rvert^2$	TM, $\lvert B_0^{II}\rvert^2$	TM, $\lvert B_1^{II}\rvert^2$	TM, $\lvert F_0^{III}\rvert^2$
ME	$4.9 \cdot 10^{-3}$	$1.8 \cdot 10^{-4}$	0.95	$1.1 \cdot 10^{-3}$	$7.5 \cdot 10^{-4}$	0.96
FDTD	$4.8 \cdot 10^{-3}$	$0.5 \cdot 10^{-4}$	0.94	$1.1 \cdot 10^{-3}$	$8.9 \cdot 10^{-4}$	0.94

(c) Junction ii, $F_0^{II} = 1/\sqrt{2}$, $F_1^{II} = -1/\sqrt{2}$:

	TE, $\lvert B_0^{II}\rvert^2$	TE, $\lvert B_1^{II}\rvert^2$	TE, $\lvert F_0^{III}\rvert^2$	TM, $\lvert B_0^{II}\rvert^2$	TM, $\lvert B_1^{II}\rvert^2$	TM, $\lvert F_0^{III}\rvert^2$
ME	$9.5 \cdot 10^{-2}$	$5.6 \cdot 10^{-2}$	$5.3 \cdot 10^{-4}$	$3.1 \cdot 10^{-2}$	$1.6 \cdot 10^{-2}$	$5.4 \cdot 10^{-4}$
FDTD	$9.1 \cdot 10^{-2}$	$5.4 \cdot 10^{-2}$	$1.0 \cdot 10^{-4}$	$3.2 \cdot 10^{-2}$	$1.6 \cdot 10^{-2}$	$5.5 \cdot 10^{-4}$

Table 1: Relative guided mode powers for the simualtion of isolated waveguide junctions corresponding to the plots of Figure 3. ME indicates the values computed with the mode expansion technique as formulated in this paper, the rows FDTD contain the results of finite difference time-domain beam propagation simulations [27]. For (a), the overlap model Eq. (7) predicts $\lvert F_0^{II}\rvert^2 = \lvert F_1^{II}\rvert^2 = 0.47$ (TE) and 0.48 (TM), correspondingly $\lvert F_0^{III}\rvert^2 = 0.95$ (TE), and 0.96 (TM) for (b), and $\lvert F_0^{III}\rvert^2 = 0$ for (c).

poorly, due to the artificial reflections from the window boundaries. 20 expansion terms is also not enough to adequately decompose the adjacent fields in the plane of the junction: discontinuities e.g. in the longitudinal

component of the Poynting vector are clearly visible in $z = 0$. Note that the mismatch of the guided parts of the fields, and consequently the fractions of radiated power, are substantial in the configurations we are interested in. If the fields belonging to the open structure are to be approximated at some z-distances on both sides of the junction, a larger computational window is advisable, and this in turn requires to take more basis functions into account.

Another (serious) reason for placing the artificial walls far apart is the "windowing error" which leads to a oscillating type of convergence, if one considers e.g. a plot of the mode reflection coefficients, converged with respect to the number of mode terms, versus the width of the computational window. These oscillations are observed with the present approach; see Refs. [28, 24] for more details.

Our implementation does not employ any kind of transparent or absorbing boundary conditions. Despite the computational effort in terms of a wide window and large basis sets, the (squared) propagation constants have to be searched on the real axis only. Hence the algorithm is likely to be much more stable and efficient than one which searches wavenumbers in the complex plane (this would be necessary if complex refractive indices are involved). However, simulating a long structure requires specific measures, as explaned in Section 5.

To verify the our analysis, we have applied the finite difference time domain beam propagation technique described in Ref. [27, 29] and found a reasonable agreement. Table 1 compares the results. The spatially two-dimensional simulations rely on regular meshes of 300×400 points (TE) and 240×400 points (TM), with stepsizes of 16 nm (TE) and 19 nm (TM) for the x-direction and 20 nm for the z-direction. The boundaries of the computational window ($-2.6\,\mu m \leq x \leq 2.3\,\mu m$ (TE), $-1.9\,\mu m \leq x \leq 2.7\,\mu m$ (TM), $-4\,\mu m \leq z \leq 4\,\mu m$) are fitted with perfectly matched layers [29] to cope with the outgoing radiation.

5 Cross strip interferometer: Rigorous mode expansion

As demonstrated by the plots of Figure 3, the nonguided parts of the field that initiate from the junctions at $z = 0$ rapidly leave the film region with growing propagating distance $\pm z$. While in the real open structure there is no physical reason why this power should return, the boundaries introduced for the mode expansion will reflect these fields back into the region of the waveguide, if the model would be applied unmodified to the entire interferometer.

Observing that segment II is usually much longer than a typical distance on which the radiation leaves the waveguide, the obstacle can be circumvented in the following way. The forward traveling field on the right side of junction i consists of two guided modes and a remainder. The remainder, representing the diverging radiation field, is neglected for the simulation of junction ii, where only the two guided modes are assumed to be coming in from segment II. Likewise, the backward traveling field initiating from junction ii is split into a guided part, which excites junction i from the right, and a nonguided part, which crosses the plane $z = 0$ sufficiently far away from the waveguide. Thus these nonguided modes are negligible for the simulation of junction i. Note that dropping the fields requires a homogeneous waveguide segment of a certain length between the two junctions. It is clearly not applicable e.g. in the case of a grating, where usually the period is in the order of the wavelength (cf. the remarks in [26]).

To check the approximation, we have summed the intensity on the relevant vertical boundaries $z = 2.5\,\mu m$ (a), $z = -2.5\,\mu m$ (b, c), $-1.5\,\mu m < x < 1.5\,\mu m$, of the plots of Figure 3 with the amplitudes of the guided modes set to zero. In all six cases the relative power related to the nonguided fields close to the waveguide was below 0.02, indicating that these fields, if allowed to propagate freely over the entire length L of the strip (see Table 2), would well have left the x-region which is relevant for the junction modeling.

The above reasoning allows to apply the mode expansion technique to the long cross strip. We have to simulate the two junctions simultaneously, with separate radiation fields, but with the guided fields mediating between them. Using the notation of Section 4, the field in segments I and III is expanded into the local modes (5) with relative amplitude vectors $\boldsymbol{f}^{I}$, $\boldsymbol{b}^{I}$, and $\boldsymbol{f}^{III}$, $\boldsymbol{b}^{III}$, which contain the mode amplitudes in the plane $z = 0$ on the left side of junction i, and in the plane $z = L$ on the right side of junction ii, respectively. For segment II, two sets of amplitudes $\boldsymbol{f}^{II}_{i,g}$, $\boldsymbol{f}^{II}_{i,r}$, $\boldsymbol{b}^{II}_{i,g}$, $\boldsymbol{b}^{II}_{i,r}$, and $\boldsymbol{f}^{II}_{ii,g}$, $\boldsymbol{f}^{II}_{ii,r}$, $\boldsymbol{b}^{II}_{ii,g}$, $\boldsymbol{b}^{II}_{ii,r}$ collect the amplitudes of the guided (index g) and nonguided modes (index r) on the right side of junction i (index i) and on the left side of junction ii (index ii).

Bidirectional projection relates these quantities by transfer matrices M^{I}, M^{II}, and Q^{II}, $\mathsf{Q}^{\mathrm{III}}$, where the latter are the equivalents of the operators in Eq. (10) for junction ii. Splitting the transfer matrices into suitable parts, this reads

$$
\begin{pmatrix} \boldsymbol{f}^{\mathrm{I}} \\ \boldsymbol{b}^{\mathrm{I}} \end{pmatrix} = \begin{pmatrix} \mathsf{M}^{\mathrm{I}}_{\mathrm{ffg}} & \mathsf{M}^{\mathrm{I}}_{\mathrm{ffr}} & \mathsf{M}^{\mathrm{I}}_{\mathrm{fbg}} & \mathsf{M}^{\mathrm{I}}_{\mathrm{fbr}} \\ \mathsf{M}^{\mathrm{I}}_{\mathrm{bfg}} & \mathsf{M}^{\mathrm{I}}_{\mathrm{bfr}} & \mathsf{M}^{\mathrm{I}}_{\mathrm{bbg}} & \mathsf{M}^{\mathrm{I}}_{\mathrm{bbr}} \end{pmatrix} \begin{pmatrix} \boldsymbol{f}^{\mathrm{II}}_{\mathrm{i,g}} \\ \boldsymbol{f}^{\mathrm{II}}_{\mathrm{i,r}} \\ \boldsymbol{b}^{\mathrm{II}}_{\mathrm{i,g}} \\ \boldsymbol{b}^{\mathrm{II}}_{\mathrm{i,r}} \end{pmatrix}, \qquad \begin{pmatrix} \boldsymbol{f}^{\mathrm{II}}_{\mathrm{i,g}} \\ \boldsymbol{f}^{\mathrm{II}}_{\mathrm{i,r}} \\ \boldsymbol{b}^{\mathrm{II}}_{\mathrm{i,g}} \\ \boldsymbol{b}^{\mathrm{II}}_{\mathrm{i,r}} \end{pmatrix} = \begin{pmatrix} \mathsf{M}^{\mathrm{II}}_{\mathrm{fgf}} & \mathsf{M}^{\mathrm{II}}_{\mathrm{fgb}} \\ \mathsf{M}^{\mathrm{II}}_{\mathrm{frf}} & \mathsf{M}^{\mathrm{II}}_{\mathrm{frb}} \\ \mathsf{M}^{\mathrm{II}}_{\mathrm{bgf}} & \mathsf{M}^{\mathrm{II}}_{\mathrm{bgb}} \\ \mathsf{M}^{\mathrm{II}}_{\mathrm{brf}} & \mathsf{M}^{\mathrm{II}}_{\mathrm{brb}} \end{pmatrix} \begin{pmatrix} \boldsymbol{f}^{\mathrm{I}} \\ \boldsymbol{b}^{\mathrm{I}} \end{pmatrix}, \tag{14}
$$

$$
\begin{pmatrix} \boldsymbol{f}^{\mathrm{II}}_{\mathrm{ii,g}} \\ \boldsymbol{f}^{\mathrm{II}}_{\mathrm{ii,r}} \\ \boldsymbol{b}^{\mathrm{II}}_{\mathrm{ii,g}} \\ \boldsymbol{b}^{\mathrm{II}}_{\mathrm{ii,r}} \end{pmatrix} = \begin{pmatrix} \mathsf{Q}^{\mathrm{II}}_{\mathrm{fgf}} & \mathsf{Q}^{\mathrm{II}}_{\mathrm{fgb}} \\ \mathsf{Q}^{\mathrm{II}}_{\mathrm{frf}} & \mathsf{Q}^{\mathrm{II}}_{\mathrm{frb}} \\ \mathsf{Q}^{\mathrm{II}}_{\mathrm{bgf}} & \mathsf{Q}^{\mathrm{II}}_{\mathrm{bgb}} \\ \mathsf{Q}^{\mathrm{II}}_{\mathrm{brf}} & \mathsf{Q}^{\mathrm{II}}_{\mathrm{brb}} \end{pmatrix} \begin{pmatrix} \boldsymbol{f}^{\mathrm{III}} \\ \boldsymbol{b}^{\mathrm{III}} \end{pmatrix}, \qquad \begin{pmatrix} \boldsymbol{f}^{\mathrm{III}} \\ \boldsymbol{b}^{\mathrm{III}} \end{pmatrix} = \begin{pmatrix} \mathsf{Q}^{\mathrm{III}}_{\mathrm{ffg}} & \mathsf{Q}^{\mathrm{III}}_{\mathrm{ffr}} & \mathsf{Q}^{\mathrm{III}}_{\mathrm{fbg}} & \mathsf{Q}^{\mathrm{III}}_{\mathrm{fbr}} \\ \mathsf{Q}^{\mathrm{III}}_{\mathrm{bfg}} & \mathsf{Q}^{\mathrm{III}}_{\mathrm{bfr}} & \mathsf{Q}^{\mathrm{III}}_{\mathrm{bbg}} & \mathsf{Q}^{\mathrm{III}}_{\mathrm{bbr}} \end{pmatrix} \begin{pmatrix} \boldsymbol{f}^{\mathrm{II}}_{\mathrm{ii,g}} \\ \boldsymbol{f}^{\mathrm{II}}_{\mathrm{ii,r}} \\ \boldsymbol{b}^{\mathrm{II}}_{\mathrm{ii,g}} \\ \boldsymbol{b}^{\mathrm{II}}_{\mathrm{ii,r}} \end{pmatrix}. \tag{15}
$$

Additionally, the guided mode amplitudes at $z = 0+$ and $z = L-$ are connected by diagonal propagation matrices which include the phase velocities of the relevant modes:

$$
\boldsymbol{f}^{\mathrm{II}}_{\mathrm{ii,g}} = \mathsf{T}_{+}\boldsymbol{f}^{\mathrm{II}}_{\mathrm{i,g}}, \quad \boldsymbol{b}^{\mathrm{II}}_{\mathrm{ii,g}} = \mathsf{T}_{-}\boldsymbol{b}^{\mathrm{II}}_{\mathrm{i,g}}, \quad \text{where} \quad (\mathsf{T}_{\pm})_{lm} = \begin{cases} \mathrm{e}^{\mp \mathrm{i}\beta^{\mathrm{II}}_m L}, & \text{if } l = m, \\ 0 & \text{otherwise.} \end{cases} \tag{16}
$$

The device is to be excited by the guided mode of segment I, without any other incoming fields. This requires $f^{\mathrm{I}}_0 = \sqrt{\mathcal{P}^{\mathrm{I}}/P^{\mathrm{I}}_0}$, $f^{\mathrm{I}}_m = 0$, if $m \neq 0$, and $\boldsymbol{b}^{\mathrm{III}} = 0$. Putting $\boldsymbol{b}^{\mathrm{II}}_{\mathrm{i,r}} = 0$ and $\boldsymbol{f}^{\mathrm{II}}_{\mathrm{ii,r}} = 0$ implements the open structure for segment II, as discussed in the beginning of this section. Besides in the remaining coefficients of segment II, we are interested in the mode amplitudes $\boldsymbol{b}^{\mathrm{I}}$ and $\boldsymbol{f}^{\mathrm{III}}$ related to the reflection and transmission of the entire device, and in particular in $|B^{\mathrm{I}}_0|^2 = P^{\mathrm{I}}_0|b^{\mathrm{I}}_0|^2$ and $\mathcal{P} = |F^{\mathrm{III}}_0|^2 = P^{\mathrm{III}}_0|f^{\mathrm{III}}|^2$, the guided reflected and transmitted power.

Solving the system (14), (15), and (16) with the above constraints results in the expressions

$$
\boldsymbol{f}^{\mathrm{III}} = \left(\mathsf{D} - \mathsf{F}\mathsf{A}^{-1}\mathsf{B}\right)^{-1} \left(\mathsf{E} + \mathsf{F}\mathsf{A}^{-1}\mathsf{C}\right) \boldsymbol{f}^{\mathrm{I}} \quad \text{and} \quad \boldsymbol{b}^{\mathrm{I}} = \mathsf{A}^{-1}\mathsf{B}\boldsymbol{f}^{\mathrm{III}} + \mathsf{A}^{-1}\mathsf{C}\boldsymbol{f}^{\mathrm{I}} \tag{17}
$$

with

$$
\begin{aligned}
\mathsf{A} &= 1 - \mathsf{M}^{\mathrm{I}}_{\mathrm{bfr}} \mathsf{M}^{\mathrm{II}}_{\mathrm{frb}}, \\
\mathsf{B} &= \mathsf{M}^{\mathrm{I}}_{\mathrm{bfg}} \mathsf{T}_{-} \mathsf{Q}^{\mathrm{II}}_{\mathrm{fgf}} + \mathsf{M}^{\mathrm{I}}_{\mathrm{bbg}} \mathsf{T}_{+} \mathsf{Q}^{\mathrm{II}}_{\mathrm{bgf}}, \\
\mathsf{C} &= \mathsf{M}^{\mathrm{I}}_{\mathrm{bfr}} \mathsf{M}^{\mathrm{II}}_{\mathrm{frf}}, \\
\mathsf{D} &= 1 - \mathsf{Q}^{\mathrm{III}}_{\mathrm{fbr}} \mathsf{Q}^{\mathrm{II}}_{\mathrm{brf}}, \\
\mathsf{E} &= \mathsf{Q}^{\mathrm{III}}_{\mathrm{ffg}} \mathsf{T}_{+} \mathsf{M}^{\mathrm{II}}_{\mathrm{fgf}} + \mathsf{Q}^{\mathrm{III}}_{\mathrm{fbg}} \mathsf{T}_{-} \mathsf{M}^{\mathrm{II}}_{\mathrm{bgf}}, \\
\mathsf{F} &= \mathsf{Q}^{\mathrm{III}}_{\mathrm{ffg}} \mathsf{T}_{+} \mathsf{M}^{\mathrm{II}}_{\mathrm{fgb}} + \mathsf{Q}^{\mathrm{III}}_{\mathrm{fbg}} \mathsf{T}_{-} \mathsf{M}^{\mathrm{II}}_{\mathrm{bgb}},
\end{aligned} \tag{18}
$$

which are directly suitable for a numerical implementation.

6 Polarizer design

The discussion shall be restricted to a device that transmits as much as possible of the power related to TE polarized input light, while it blocks TM throughput. The polarizer has to be characterized in terms of the polarization discrimination or extinction ratio $\mathrm{ER} = 10\log_{10} \mathcal{P}^{\mathrm{TE}}/\mathcal{P}^{\mathrm{TM}}$ and the insertion loss $\mathrm{LO} = -10\log_{10} \mathcal{P}^{\mathrm{TE}}$, where $\mathcal{P}^{\mathrm{TE}}$ and $\mathcal{P}^{\mathrm{TM}}$ are the relative TE and TM power transmissions.

For the cross strip geometry with given material parameters and wavelength, the design starts with identifying a proper total thickness t and length L of the strip. The overlap model of Section 3 predicts periodic variations in the power transfer as a function of L with different beat lengths $L^{\mathrm{TE}}_{\mathrm{c}}$ and $L^{\mathrm{TM}}_{\mathrm{c}}$. Polarizer performance

requires a (short) configuration, where L is an even multiple of L_c^{TE} and simultaneously an odd multiple of L_c^{TM}. For a difference of one in the multiplicities, these conditions fix the optimum polarizer length as $L_p = L_c^{TE} L_c^{TM} / (L_c^{TE} - L_c^{TM})$. By varying t over the range where segment II supports two guides modes for both polarizations, evaluating L_p and checking for an even integer L_p / L_c^{TE}, one can indeed find a suitable geometry. Figure 4 shows the resulting dependence of the characteristic quantities on the strip length. At the proper length $L_p = 4L_c^{TE} = 5L_c^{TM}$, the transmission curves related to TE and TM polarization achieve their maximum or minimum, respectively. Note that a multiplicity difference of one in the coupling lengths does not only lead to the shortest possible device, but also to the most relaxed fabrication tolerances. The allowed intervals for parameter deviations are roughly inversely proportional to the overall device length, see Ref. [30].
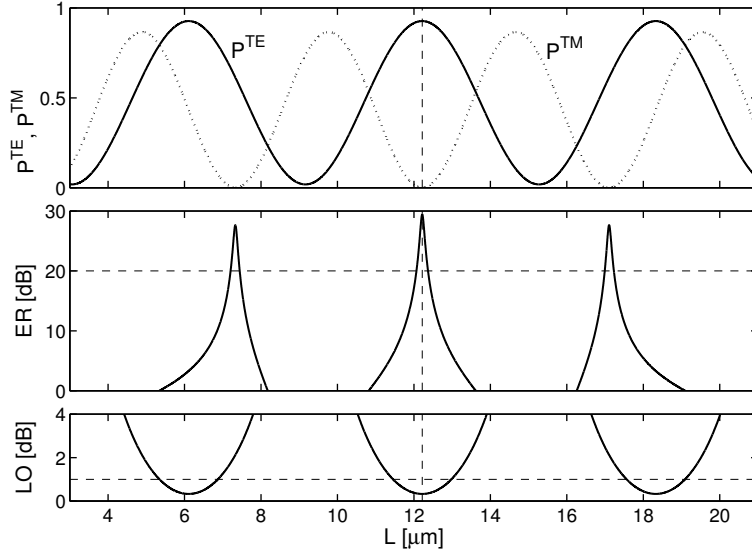
Figure 4: TE and TM power transmissions $\mathcal{P}^{TE}$, $\mathcal{P}^{TM}$, polarization discrimination ER and loss LO versus the length L of the thick segment. Parameters are as stated in Table 2. The vertical line identifies the best polarizer length $L_p = 12.218\,\mu m$, an integer multiple of the beat lengths $L_c^{TE} = 3.054\,\mu m$ and $L_c^{TM} = 2.444\,\mu m$.

The design proceeds with the search for a suitable etching depth h. Figure 5 compares corresponding data calculated with the approximate expression (8) on the one hand, and according to Eq. (17) on the other. A difference is hardly visible on the linear power scale, but becomes apparent on the logarithmic scale of the extinction ratio. While the polarization discrimitation is unlimited in the simple model (w_0^{TM} and w_1^{TM} become equal), according to the mode expansion an ideal polarizer can not be expected. However, the optimum performance, reached for an etching depth that is slightly different from the prediction of (8), is still quite reasonable.
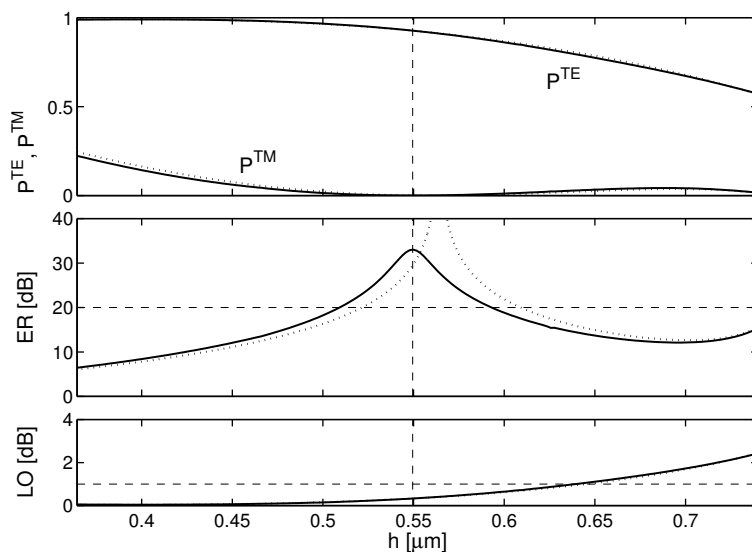

Figure 5: TE and TM power transmissions $\mathcal{P}^{TE}$, $\mathcal{P}^{TM}$, polarization discrimination ER and loss LO versus the etching depth h, for structures given by the parameters of Table 2. The dotted lines are the results of the rough overlap model; rigorous mode expansion leads to the continuous curves.

Table 2 summarizes the parameters of the resulting polarizer proposal. For the tuned device, a simulation as described in Section 5 with 400 expansion terms on a window $-15\,\mu m \leq x \leq 10\,\mu m$ for each segment predicts relative power throughputs of $\mathcal{P}^{TE} = 93\%$ and $\mathcal{P}^{TM} = 0.035\%$. This amounts to a polarization discrimination

ER $= 34\,$dB and an insertion loss LO $= 0.33\,$dB. Relative guided powers of 0.07% (TE) and 5.9% (TM) are reflected. Plots of the corresponding fields in Figure 6 illustrate the behaviour of the interferometer.

	t	h	L	λ	n_{s}	n_{f}	n_{c}
q	$0.962\,\mu$m	$0.549\,\mu$m	$12.218\,\mu$m	$1.3\,\mu$m	1.5	2.0	1.0
$\Delta q^{(1)}$	$8\,$nm	$60\,$nm	$0.15\,\mu$m	$32\,$nm	0.016	0.026	0.060
$\Delta q^{(2)}$	$18\,$nm	$34\,$nm	$0.39\,\mu$m	$65\,$nm	0.040	0.071	0.192

Table 2: *Structural parameters q and tolerances Δq for a planar polarizer as sketched in Figure 1. $\Delta q^{(1)}$ ($\Delta q^{(2)}$) corresponds to limits for extinction ratio and loss of 20 dB and 1 dB (10 dB and 0.5 dB). See the text for a concise interpretation of the fabrication tolerances.*

The tolerances given in Table 2 indicate that the polarizer should still achieve an extinction ratio higher than $20\,$dB ($10\,$dB) and suffer from losses below $1\,$dB ($0.5\,$dB), if a single parameter deviates from the optimum value q by not more than $\pm\Delta q$. These limits are estimated with the help of Eq. (8). A change in h alters the overlaps w_m only, while a change in t affects the propagation constants β_m^{II} as well. Hence the device turns out to be more sensitive with respect to the total thickness (and the strip length L) than with respect to the etching depth.
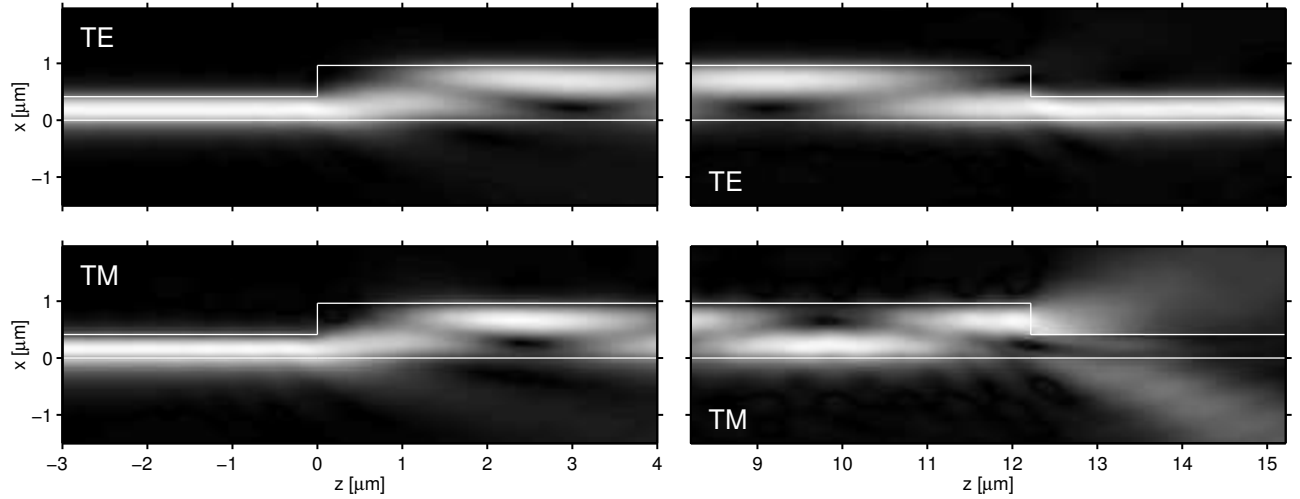

Figure 6: *Simulation of the light propagation through the cross strip defined by Table 2, for TE (top) and TM polarized input (bottom). For TE polarization, almost the entire power passes the device smoothly, while the second junction scatters TM polarized waves into the surrounding.*

E.g. from Ref. [31] one can obtain hints regarding the criticalness of the thickness t, the geometric parameter with the narrowest tolerance interval. Typical growth rates for Silicon Oxynitride layers are about $5\,$nm$/$min, with a nonuniformity as low as 0.5% on a $2\,$cm$\times 2\,$cm area, implying deviations of about $5\,$nm for $t = 0.962\,\mu$m. Demanding the thickness to be within the $16\,$nm interval that is stated in row $\Delta q^{(1)}$ of Table 2 seems reasonable.

Cascading the cross strips may be a means to relax the tolerance requirements. Row $\Delta q^{(2)}$ of Table 2 can be interpreted in that way. Disregarding reflections and assuming a sufficient distance between them, a sequence of two polarizer strips with $10\,$dB extinction ratio and $0.5\,$dB loss should perform like a single $20\,$dB$/1\,$dB device. With the exception of h (here the loss is the limiting constraint, see Figure 5), the tolerance requirements for the single strips are indeed considerably relaxed, while the overall length can be still small, say $50\,\mu$m.

In terms of the interferometer performance discussed in Section 5, the geometry is suboptimal for both TE and TM polarizations: If L would be allowed to vary, then $\mathcal{P}^{\mathrm{TM}}$ reaches up to 85% only, while $\mathcal{P}^{\mathrm{TE}}$ does not fall below 1.9%. Hence a TM-transparent polarizer requires a resized geometry (suitable dimensions are $t = 0.870\,\mu$m, $h = 0.580\,\mu$m, and $L = 34.150\,\mu$m for otherwise unchanged parameters), not only a modified length.

The material parameters as stated in Table 2 resemble typical values for Silicon-Nitride / Silicon-Oxide waveguides [31]. Usually these are grown on a Silicon substrate. Provided that the SiO$_2$ buffer layer is sufficiently thick, one may neglect the presence of the Silicon below the waveguide, as we have done before. Note that

the presence of the real substrate is not likely to affect the polarizer performance: The largest part of the downwards radiated fields disappears directly into the high index Silicon. The reflected part may reenter the waveguide region, but, being composed of modes that are orthogonal to the guided output mode, the fields cross the waveguide and dissapear into the cover. Or the power is again reflected into the direction of the substrate. Provided that the output segment is of a sufficient length, the power throughput should be indeed equal to the coefficient $|F_0^{\mathrm{III}}|^2$.

An extension of the present planar design to channel waveguides will be a subject of future research. Suitable annealing or etching a shallow rib could be means to create a laterally weakly confining waveguide across the strip. This seems to be unlikely to disturb the properties of the interferometer significantly.

7 Conclusions

A thicker, bimodal segment of specific length and height between two single mode sections of a planar waveguide can serve as a simple interferometer. Depending on the phase gain of the two modes in the intermediate region, the fields interfere almost completely destructively, or constructively with relatively low losses. The structure unifies some features of a two-dimensional directional coupler missing a gap, and of a multimode interference device involving only two modes.

Considering only overlaps of forward propagating modes gives a basic insight into the behaviour of the interferometer, and allows one to isolate suitable parameter sets. We have assessed and optimized the device performance in terms of a rigorous mode expansion model, including radiation and reflection. Despite the abrupt waveguide discontinuities, we have found only moderate levels of reflections for tuned configurations.

Such a cross strip interferometer can be dimensioned to perform as a very short integrated optical polarizer. We have simulated a device that suppresses TM polarization in Silicon-based waveguides; the proposal is easily transferable to other materials and to TE suppression.

Acknowledgment

References

[1] M. A. Sletten and S. R. Seshadri. Thick metal surface-polariton polarizer for a planar optical waveguide. *Journal of the Optical Society of America A*, 7(7):1174–1184, 1990.

[2] M. Saini, E. K. Sharma, and M. Singh. Strong effect of output coupling on the performance of metal-clad waveguide polarizers. *Optics Letters*, 20(4):365–367, 1995.

[3] D. L. Veasey, R. K. Hickernell, D. R. Larson, and T. E. Batchman. Waveguide polarizers with hydrogenated amorphous silicon claddings. *Optics Letters*, 16(10):717–719, 1991.

[4] D. L. Veasey, D. R. Larson, and I. Veigl. Waveguide polarizers processed by localized plasma etching. *Applied Optics*, 33(7):1242–1244, 1994.

[5] W. Johnstone, G. Stewart, T. Hart, and B. Culshaw. Surface plasmon polaritons in thin metal films and their role in fiber optic polarizing devices. *Journal of Lightwave Technology*, 8(4):538–544, 1990.

[6] K. Thyagarajan, S. Diggavi, A. K. Ghatak, W. Johnstone, G. Stewart, and B. Culshaw. Thin-metal-clad waveguide polarizers: analysis and comparison with experiment. *Optics Letters*, 15(18):1041–1043, 1990.

[7] T. Nakano, K. Baba, and M. Miyagi. Insertion loss and extinction ratio of a surface plasmon-polariton polarizer: theoretical analysis. *Journal of the Optical Society of America A*, 11(10):2030–2035, 1994.

[8] M. J. Bloemer and J. W. Haus. Compact, high-extinction waveguide polarizers that use localized surface plasmons. *Optics Letters*, 17(8):598–600, 1992.

[9] M. J. Bloemer and J. W. Haus. Versatile waveguide polarizer incorporating an ultrathin discontinuous silver film. *Applied Physics Letters*, 61(14):1619–1621, 1992.

[10] M. J. Bloemer and J. W. Haus. Broadband waveguide polarizers based on the anisotropic optical constants of nanocomposite films. *Journal of Lightwave Technology*, 14(6):1534–1540, 1996.

[11] T. Findakly, B. Chen, and D. Booher. Single-mode integrated-optical polarizers in LiNbO$_3$ and glass waveguides. *Optics Letters*, 8(12):641–643, 1983.

[12] K. Thyagarajan, S. D. Seshadri, and A. K. Ghatak. Waveguide polarizer based on resonant tunneling. *Journal of Lightwave Technology*, 9:315–317, 1991.

[13] C. S. Pérez, A. Morand, P. Benech, S. Tedjini, D. Bosc, and A. Rousseau. Low cost integrated optical polarizer with an hybrid structure of birefringent polymer and ion-exchanged glass waveguide. In G. C. Righini and S. I. Najafi, editors, *Integrated Optics Devices III*, volume 3620 of SPIE Proceedings, pages 118–125, 1999.

[14] U. Hempelmann, H. Herrmann, G. Mrozynski, V. Reimann, and W. Sohler. Integrated optical proton exchanged TM-pass polarizers in LiNbO$_3$: modelling and experimental performance. *Journal of Lightwave Technology*, 13(8):1750–1759, 1995.

[15] M.-C. Oh, S.-Y. Shin, W.-Y. Hwang, and J.-J. Kim. Poling-induced waveguide polarizers in electrooptic polymers. *IEEE Photonics Technology Letters*, 8(3):375–377, 1996.

[16] K. G. Han, S. Kim, and S. S. Choi. Controllable integrated-optic polarization splitter-combiner. *Optics Letters*, 15(2):108–109, 1990.

[17] L. Bersiner, U. Hempelmann, and E. Strake. Numerical analysis of passive integrated-optical polarization splitters: comparison of finite-element method and beam-propagation method results. *Journal of the Optical Society of America B*, 8(2):422–433, 1991.

[18] Y. Shani, C. H. Henry, R. C. Kistler, and K. J. Orlowsky. Four-port integrated optic polarization splitter. *Applied Optics*, 29(3):337–339, 1990.

[19] K. G. Han, D. H. Kim, J. C. Jo, and S. S. Choi. Ti:LiNbO$_3$ polarization splitters using an asymmetric branching waveguide. *Optics Letters*, 16(14):1086–1088, 1991.

[20] K. Thyagarajan and S. Pilevar. Resonant tunneling three-waveguide polarization splitter. *Journal of Lightwave Technology*, 10:1334–1337, 1992.

[21] U. Trutschel, F. Ouelette, V. Delisle, M. A. Duguay, G. Fogarty, and F. Lederer. Polarization splitter based on antiresonant reflecting optical waveguides. *Journal of Lightwave Technology*, 13:239–243, 1995.

[22] M. Lohmeyer, N. Bahlmann, O. Zhuromskyy, and P. Hertel. Radiatively coupled waveguide polarization splitter simulated by wave-matching based coupled mode theory. *Optical and Quantum Electronics*, 31:877–891, 1999.

[23] S. S. Lee, S. Garner, W. H. Steier, and S. Y. Shin. Integrated optical polarization splitter based on photobleaching-induce birefringence in azo dye polymers. *Applied Optics*, 38(3):530–533, 1999.

[24] C. Vassallo. *Optical Waveguide Concepts*. Elsevier, Amsterdam, 1991.

[25] G. Sztefka and H. P. Nolting. Bidirectional eigenmode propagation for large refractive index steps. *IEEE Photonics Technology Letters*, 5(5):554–557, 1993.

[26] J. Willems, J. Haes, and R. Baets. The bidirectional mode expansion method for two-dimensional waveguides: the TM case. *Optical and Quantum Electronics*, 27:995–1007, 1995.

[27] R. Stoffer, H. J. W. M. Hoekstra, R. M. de Ridder, E. van Groesen, and F. P. H. van Beckum. Numerical studies of 2D photonic crystals: Waveguides, coupling between waveguides and filters. *Optical and Quantum Electronics*, 32:947–961, 2000.

[28] G. H. Brooke and M. M. Z. Kharadly. Scattering by abrupt discontinuities on planar dielectric waveguides. *IEEE Transactions on Microwave Theory and Techniques*, MTT-30:760–770, 1982.

[29] A. Taflove. *Computational Electrodynamis: The Finite Difference Time Domain Method*. Artech House Inc., Norwood, MA, USA, 1995.

[30] M. Lohmeyer, N. Bahlmann, and P. Hertel. Geometry tolerance estimation for rectangular dielectric waveguide devices by means of perturbation theory. *Optics Communications*, 163(1-3):86–94, 1999.

[31] K. Wörhoff, P. V. Lambeck, H. Albers, O. F. J. Noordman, N. F. van Hulst, and Th. J. A. Popma. Optimization of LPCVD Silicon Oxynitride growth to large refractive index homogeneity and layer thickness uniformity. In O. M. Parriaux, E. B. Kley, B. Culshaw, and M. Breidne, editors, *Micro-optical Technologies for Measurement, Sensors, and Microsystems II*, volume 3099 of SPIE Proceedings, pages 257–268, 1997.